Hybrid Lattice Boltzmann-finite difference model for low mach number combustion simulation

A. Hosseini, S., Hesam Safari, Nasser Darabiha, Dominique Thévenin, Manfred Krafczyk

Version of Record: https://www.sciencedirect.com/science/article/pii/S0010218019303517
Manuscript_8728a0e9583c84235772e2bab1bb8764

Hybrid Lattice Boltzmann-Finite Difference model for low Mach number combustion simulation

S.A. Hosseini[a,b,c,*], H. Safari[d], N. Darabiha[b], D. Thévenin[a], M. Krafczyk[d]

[a] *Laboratory of Fluid Dynamics and Technical Flows, University of Magdeburg "Otto von Guericke", D-39106 Magdeburg, Germany*
[b] *Laboratoire EM2C, CNRS, CentraleSupélec, Université Paris-Saclay, 3 rue Joliot Curie, 91192, Gif-sur-Yvette Cedex, France*
[c] *International Max Planck Research School (IMPRS) for Advanced Methods in Process and Systems Engineering, Magdeburg, Germany*
[d] *Institute for Computational Modeling in Civil Engineering, Technische Universität Braunschweig, Germany*

Abstract

A hybrid Lattice Boltzmann(LB)-Finite Difference(FD) numerical scheme for the simulation of reacting flows at low Mach numbers is presented. The FD solver is used to model the energy and species fields while the LB model computes the flow field. The proposed LB solver is a modified version of the classical iso-thermal weakly compressible LB scheme with the hydrodynamic pressure as its zeroth-order moment instead of density, recovering the well-known low Mach number approximation for thermo-compressible flows. The proposed numerical approach is used to model a variety of test-cases ranging from 1-D to 3-D configurations, involving premixed and non-premixed flames. In all cases results obtained by this solver are shown to agree very well with reference data.

Keywords: Lattice Boltzmann, Finite Difference, Combustion, Thermal Dilatation, Detailed Thermo-Chemical Models
2010 MSC: 00-01, 99-00

1. Introduction

The lattice Boltzmann (LB) method, proposed in the early 80's has grown very popular during the past decades. The rapid emergence of this numerical method is mainly due to the simplicity and strict locality of the involved time-evolution operators. The locality of the operators and intrinsic coupling between the pressure and velocity fields through the distribution function, as opposed to pressure-based incompressible or low Mach solvers allows for better performances on parallel clusters and a much more efficient treatment of

*Corresponding author
Email address: seyed.hosseini@ovgu.de (S.A. Hosseini)

flows in complex geometries [1]. During the past decade, the LB method for computational fluid dynamics (CFD) has been extended to many complex flow configurations ranging from non-Newtonian [2], to multi-phase [3, 4, 5, 6, 7] and multi-component flows. Although initially limited to low-Mach iso-thermal flows with an ideal gas equation of state, the LB approach was later modified to lift many of these restrictions. Releasing the restriction on thermo-compressibility is an essential step to develop LB solvers for many applications such as reacting flows at low Mach numbers.

The topic of low-Mach combustion modeling with LB was first touched upon in 1997 in an article by Succi et al. [8]. Since then a limited number of publications have appeared on the topic, all limited to simplified 1 and 2-D test-cases. To go from the classical LB formulation to one adapted to combustion simulation, one must take into account additional independent fields – i.e., species mass fractions and energy– and consistently couple them. As a side-note, it is also worth mentioning that stability might become a major restriction with the single relaxation time collision operator when confronted to such flows. This issue has been dealt with to some extent through a variety of more advanced collision operators, e.g. multiple relaxation time [9, 10], central moments or cascaded LB [11, 12, 13, 14], Cumulants [15, 16, 17, 18], regularized [19, 20] and Entropic [21, 22]. The issue of stability will not be treated here as it is not the focus of the article. As such the single relaxation time collision operator will be used. To date, two main categories of solvers, either purely or partially based on the LB formulation, have been proposed in the literature. In the context of the present work these categories will be referred to as : (1) single-fluid and (2) multi-fluid models.

The latter formulation comprises a set of N_{sp} distribution functions (one for each species present in the flow) solving the corresponding set of continuity and Navier-Stokes-Fourier equations for each species. Inter-species interactions such as mass diffusion are modeled through appropriate collision operators. Notable examples of such formulations can be seen, for instance, in [23, 24, 25, 26, 27]. The models proposed in [23, 24, 25] are based on the standard LB discretization of velocity and physical space, standard first-neighbour stencils and equilibrium distribution function (EDF) for each component supplemented with a slow/fast manifold decomposition of the collision operator using a quasi-equilibrium state allowing for independent viscosity and mass diffusion coefficients. Furthermore, as the populations do not necessarily propagate on-lattice the standard collision and streaming is followed by an interpolation step. As the standard stencils do not correctly recover the higher order moments (at third- and fourth-orders), correction terms are added to the equations. On the other hand the approach proposed in [26, 27, 28, 29] relies on different velocity and time-space discretization strategies. The discrete phase-space and the EDF are constructed using the moment-matching method, while physical space and time are discretized using the finite difference (FD) method. The larger velocity stencil employed allows for the model to correctly recover higher order moments, and capture non-equilibrium effects. While decoupling time and space discretization from phase-space, thus potentially facilitating simulations at higher Mach numbers

and with large temperature variations, the classical space discretization of the hyperbolic system of equations comes at a higher cost–compared to the LB algorithm.
The first category carries the "single-fluid" denomination because just like classical CFD solvers, a single so-called "mixture-averaged" set of NS and energy balance equations are solved. These are supplemented with a balance equation for each one of the chemical species involved in the flow. While the flow solver is based on the LB method in all cases, the additional fields can be solved using various LB formulations [30, 31, 32, 33] or classical solvers for the macroscopic balance equations. The so-called "Advection-Diffusion" LB formulation has usually been employed to model the additional fields. Contrary to multi-fluid solvers, the additional LB solvers only need to correctly recover the zeroth, first and second-order moments, and therefore require fewer discrete velocities. In its classical form, this formulation comes with a number of restriction, e.g. incompressible flow, generalized Fick approximation for the diffusion term etc, that have to be dealt with [34]. Extensions to this model allowing to incorporate more complex physics and variable density for the species, and variable specific heat capacities for the energy equation have also been developed [35, 36, 37]. The other possibility, i.e. solving the additional fields through classical solvers for the macroscopic balance equations, has also been considered in a number of publications[38, 39]. The choice of the solver for the additional fields (i.e., species and energy), and a comparative performance study of these approaches is not as straightforward as for the flow solver as no velocity-pressure-type coupling issues for the species and temperature fields are encountered. The comparison is even more subtle as due to the reduced number of conserved moments the memory consumption of the LB solver is drastically reduced and becomes comparable to its FD counter-part. Furthermore, the LB formulation results in a slightly extended linear stability domain compared to a second-order FD scheme [40]. However, some researchers have reported computational efficiency gains when replacing the LB solver with a finite difference solver. In [41], a factor of 1.5 is reported when using a Rung-Kutta scheme in combination with a finite difference solver. The main restriction at this point, for LB advection-diffusion-based solvers for the additional fields is related to stability issues for vanishing non-dimensional diffusion coefficients and the recovered physics. As mentioned previously and reported in [35, 36, 37], incorporation of more complex models, better-suited for combustion simulations, in these solvers is currently under investigation. As such in the present article, an FD solver will be used to model the species and temperature fields.
Of the limited number of LB-based articles on combustion field simulation, the majority were restricted to the *cold flame approximation*, where the flow field is decoupled from energy and species (no thermal dilatation). The coupling of energy and species fields can be seen by looking at the compressible NS equa-

tions:

$$\frac{\partial \rho u_i}{\partial t} + \frac{\partial \rho u_i u_j}{\partial x_j} + \frac{\partial p}{\partial x_i} - \frac{\partial}{\partial x_j}\left[\mu\left(\frac{\partial u_i}{\partial x_j} + \frac{\partial u_j}{\partial x_i}\right)\right] - \frac{\partial}{\partial x_i}\left[\left(\zeta - \frac{2}{3}\mu\right)\frac{\partial u_j}{\partial x_j}\right] = 0, \quad (1)$$

where here and in the rest of this article Einstein's convention for repeated indices is used. The symbols μ and ζ respectively denote the shear and bulk viscosities, the pressure p is related to local density ρ and temperature through the equation of state, and u_i is the i^{th} component of the fluid velocity vector. The shortcomings of the classical LB formulation for thermo-compressible flow simulations are two-fold. In classical LB schemes, the solver being based on the *iso-thermal* Hermite expansion of the continuous EDF around a reference stencil sound speed $c_s = \sqrt{\frac{k_B T_0}{3m_0}}$, where k_B is Boltzmann's constant, T_0 is a reference temperature and m_0 is a reference molecular mass [42]. The pressure is only function of local density and of the said reference sound speed, i.e. $p = \rho c_s^2$. Furthermore, due to the lack of symmetry of the classical first-neighbour stencils, the discrete EDF does not recover the correct third-order moments. On a minor note, the classical LB formulation does not account for additional degrees of freedom in poly-atomic molecules (i.e. rotational, vibrational) and as such can not correctly recover terms modeling dissipation of isotropic stress components (especially important in sudden compression and dilatation). For mono-atomic gases, the bulk viscosity (tied to isotropic stress dissipation) is equal to 0, while the LB solver recovers $\frac{2}{3}\mu$ due to the iso-thermal approximation [43].
A number of LB-based solvers have been proposed to correctly recover thermal dilatation. They have mostly taken one of two possible approaches; The first approach, a straight-forward extension of the classical weakly compressible iso-thermal LB, involves an EDF based on a *thermal* Hermite expansion of the continuous EDF around the reference sound speed, i.e. :

$$f_\alpha^{(eq)}(\mathbf{u}, \theta) = w_\alpha \rho \sum_{n=0}^{N} \frac{1}{n! c_s^{2n}} \boldsymbol{a_n^{(eq)}}(\boldsymbol{u}, \theta) : \boldsymbol{\mathcal{H}}_n(\boldsymbol{c_\alpha}), \quad (2)$$

where $\boldsymbol{a^{(n)}}$ and $\mathcal{H}^{(\mathbf{n})}$ are tensors of rank n respectively representing the n^{th} order Hermite coefficient and polynomial, $\boldsymbol{c_\alpha}$ are the discrete velocity vectors, w_α are the corresponding weights obtained from the Gauss-Hermite quadrature, $\theta = \frac{k_B T/m}{c_s^2}$ is the non-dimensional temperature, N is the order of truncation and ":" is the Frobenius inner product operator. The first few Hermite coefficients and polynomials are given as:

$$a_0^{(0)} = 1, \quad (3a)$$

$$a_i^{(1)} = u_i, \quad (3b)$$

$$a_{ij}^{(2)} = u_i u_j - c_s^2 (1 - \theta)\delta_{ij}, \quad (3c)$$

$$\mathcal{H}^{(0)}_{\alpha} = 1, \tag{4a}$$

$$\mathcal{H}^{(1)}_{\alpha,i} = c_{\alpha,i}, \tag{4b}$$

$$\mathcal{H}^{(2)}_{\alpha,ij} = c_{\alpha,i}c_{\alpha,j} - c_s^2\delta_{ij}. \tag{4c}$$

The second-order moment of this EDF being $\Pi^{(eq)}_{ij} = \rho u_i u_j + \rho c_s^2 \theta \delta_{ij}$, the correct thermal pressure is recovered at the Euler level. More details on this approach, and its coupling to FD solvers can be found in [44]. The quality of the approximation of the EDF by Hermite polynomials (using an expansion around a reference temperature and a reference frame at rest), regardless of the order of the subsequent quadrature, is very sensitive to the maximum deviation from the reference temperature. Large deviations from the reference temperature result in non-negligible errors in higher order moments. The deviations in the third-order moments tensor of the EDF are usually accounted for using appropriate correction terms in the time-evolution equations, as derived in [45] and [46]. Another way to overcome this issue is to have a Hermite polynomial expansion around the local fluid temperature and on a reference frame moving with the local fluid velocity, similar to Grad's original formulation [47], which results in local temperature and velocity-dependent abscissae in the Gauss-Hermite quadrature. This concept has been applied and used through "shifted lattices" [48] and off-lattice propagation of populations [49]. A similar on-grid formulation based on the reconstruction of the collision operator in the local velocity frame and re-scaled by the local temperature has recently been proposed in [50]. The concept of variable lattice sound speed (equivalent to off-lattice propagation with a fixed time-step) was also used in [51] in the form of a "particle characteristic temperature" (as referred to by the authors) and a variable time-step, δt defined so as to keep the distribution function streaming on-lattice.

Another approach to include thermal dilatation effects into the LB flow solver, follows the overall concepts of a formulation referred to as the "Low Mach Number Approximation" (LMNA) in classical CFD [52]. In this approach, the local pressure is decomposed into "thermodynamic" and "hydrodynamic" components ($p = p_{th} + \epsilon p_h$), the hydrodynamic component being a first-order (in ϵ, a small perturbation expansion parameter function of the flow Mach number) perturbation to the "equilibrium" thermodynamic pressure. The density is a dependent property computed through the ideal gas law and the local thermodynamic pressure (assumed to be uniform in the entire domain) and temperature. Further details on the LMNA, its derivation and application to low Mach combustion can be found, among other sources, in [53, 52, 54]. The classical LB formulation being a (weakly compressible) solver for the incompressible flow formulation (vanishing Mach number), it can be used to solve the LMNA. In LB, the diagonal components of the second-order moment tensor of the EDF acting as pressure are a linear function of density. As such, density and pressure (in LB) must be decoupled, in order to enforce temperature-dependent density in the context of a LMNA formulation. A limited number of modified EDFs have

been developed to that effect. The EDFs are usually modified to get "hydrodynamic" pressure as the zeroth-order moment (instead of density). For more details on some of these schemes, interested readers are referred to [51, 55].
This work will focus on presenting a hybrid LB-FD solver for combustion simulations able to recover the macroscopic balance equations in the context of the LMNA formulation, based on the thermo-compressible scheme proposed in [56]. The details of the numerical method are presented in section 2, while the third section presents validation test-cases along with the obtained results. The developed model is shown to be appropriate for low Mach number combustion simulations through a variety of test-cases with increasing levels of complexity.

2. Governing equations and numerical model

2.1. Flow field

Starting from the classical LB formulation, in its time and space-continuous form one gets:

$$\frac{\partial f_\alpha}{\partial t} + c_{\alpha,i}\frac{\partial f_\alpha}{\partial x_i} = \frac{1}{\tau}\left(f_\alpha^{(eq)} - f_\alpha\right) - F_i\frac{\partial f}{\partial \xi_i}, \tag{5}$$

where f_α is the distribution function, F_i the i^{th} component of the sum of body forces on the fluid element and τ is the relaxation coefficient. The last term on the RHS is a first-order approximation of the forcing term appearing in the continuous Boltzmann equation as follows:

$$F_i\frac{\partial f}{\partial \xi_i} \approx F_i\frac{\partial f^{(eq)}}{\partial \xi_i} = -\frac{\xi_i - u_i}{\rho c_s^2}F_i f^{(eq)}. \tag{6}$$

Here we have used ξ to designate the particle velocity instead of c_α as we are dealing with the phase-space continuous Boltzmann equation, and distribution function f.
Following [56, 57, 58, 59], a new distribution function, g_α is introduced as:

$$g_\alpha = c_s^2 f_\alpha + w_\alpha\left(p_h - \rho c_s^2\right). \tag{7}$$

Putting this equation back into Eq. 5 the following time-evolution equation is obtained for g_α:

$$\begin{aligned}\frac{\partial g_\alpha}{\partial t} + c_{\alpha,i}\frac{\partial g_\alpha}{\partial x_i} = \frac{1}{\tau}\left(g_\alpha^{(eq)} - g_\alpha\right) - w_\alpha c_s^2\left(\frac{\partial \rho}{\partial t} + c_{\alpha,i}\frac{\partial \rho}{\partial x_i}\right)\\ + w_\alpha\left(\frac{\partial p_h}{\partial t} + c_{\alpha,i}\frac{\partial p_h}{\partial x_i}\right) + \frac{1}{\rho}\left(c_{\alpha,i} - u_i\right)F_i f_\alpha^{(eq)}.\end{aligned} \tag{8}$$

Terms involving the time-derivative of pressure are dropped as they are negligible [55]. Furthermore the material derivative of density can be evaluated using the continuity equation as:

$$\frac{\partial \rho}{\partial t} + c_{\alpha,i}\frac{\partial \rho}{\partial x_i} = \left(c_{\alpha,i} - u_i\right)\frac{\partial \rho}{\partial x_i} - \rho\frac{\partial u_i}{\partial x_i}. \tag{9}$$

As mentioned earlier, the iso-thermal thermodynamic pressure in the classical LB affects the momentum balance equation through the second-order moment of the EDF. To take out this term and include contribution from the hydrodynamic pressure, p_h, the forcing term appearing in Eq. 8 is defined as:

$$F_i = c_s^2 \frac{\partial \rho}{\partial x_i} - \frac{\partial p_h}{\partial x_i} + F_{b,i}, \tag{10}$$

where F_b represents other body forces, such as gravity. Including this force term results in:

$$\begin{aligned}\frac{\partial g_\alpha}{\partial t} + c_{\alpha,i}\frac{\partial g_\alpha}{\partial x_i} = \frac{1}{\tau}\left(g_\alpha^{(eq)} - g_\alpha\right) + w_\alpha c_s^2 \rho \frac{\partial u_i}{\partial x_i} \\ + \left(c_{\alpha,i} - u_i\right)\left(\frac{f^{(eq)}}{\rho} - w_\alpha\right) c_s^2 \frac{\partial \rho}{\partial x_i} + \frac{f_\alpha^{(eq)}}{\rho}\left(c_{\alpha,i} - u_i\right) F_{b,i} \\ \underbrace{- \left(\frac{f^{(eq)}}{\rho} - w_\alpha\right) c_{\alpha,i}\frac{\partial p_h}{\partial x_i} + \frac{f^{(eq)}}{\rho} u_i \frac{\partial p_h}{\partial x_i}}_{\propto Ma^3}.\end{aligned} \tag{11}$$

Neglecting terms of order three in Mach, the final form of the equation is obtained:

$$\begin{aligned}\frac{\partial g_\alpha}{\partial t} + c_{\alpha,i}\frac{\partial g_\alpha}{\partial x_i} = \frac{1}{\tau}\left(g_\alpha^{(eq)} - g_\alpha\right) + w_\alpha c_s^2 \rho \frac{\partial u_i}{\partial x_i} \\ + \left(c_{\alpha,i} - u_i\right)\left(\frac{f^{(eq)}}{\rho} - w_\alpha\right) c_s^2 \frac{\partial \rho}{\partial x_i} + \frac{f_\alpha^{(eq)}}{\rho}\left(c_{\alpha,i} - u_i\right) F_{b,i}.\end{aligned} \tag{12}$$

Integrating the continuous equation along characteristic lines and introducing a change of variables, i.e. :

$$\begin{aligned}\bar{g}_\alpha = g_\alpha - \frac{\delta t}{2\tau}\left(g_\alpha^{(eq)} - g_\alpha\right) \\ - \frac{\delta t}{2}\left[w_\alpha c_s^2 \rho \frac{\partial u_i}{\partial x_i} + \left(c_{\alpha,i} - u_i\right)\left(\frac{f_\alpha^{(eq)}}{\rho} - w_\alpha\right) c_s^2 \frac{\partial \rho}{\partial x_i}\right. \\ \left. + \frac{f_\alpha^{(eq)}}{\rho}\left(c_{\alpha,i} - u_i\right) F_{b,i}\right],\end{aligned} \tag{13}$$

to make the resulting equation explicit, the following collision–streaming algorithm is obtained:

$$\begin{aligned}\bar{g}_\alpha\left(\mathbf{x}+\mathbf{c}_\alpha\delta t, t+\delta t\right)-\bar{g}_\alpha\left(\mathbf{x},t\right)=\\ \frac{\delta t}{\bar{\tau}}\left(\bar{g}_\alpha^{(eq)}\left(\mathbf{x},t\right)-\bar{g}_\alpha\left(\mathbf{x},t\right)\right)+\delta t c_s^2 w_\alpha \rho\left(\mathbf{x},t\right)\frac{\partial u_i\left(\mathbf{x},t\right)}{\partial x_i}\\ +\delta t\left(c_{\alpha,i}-u_i\left(\mathbf{x},t\right)\right)\left[\left(\frac{f_\alpha^{(eq)}\left(\mathbf{x},t\right)}{\rho\left(\mathbf{x},t\right)}-w_\alpha\right)\frac{\partial c_s^2\rho\left(\mathbf{x},t\right)}{\partial x_i}\right.\\ \left.+F_{b,i}\frac{f_\alpha^{(eq)}\left(\mathbf{x},t\right)}{\rho\left(\mathbf{x},t\right)}\right], \quad (14)\end{aligned}$$

where δt and δx are respectively the time-step and grid sizes, and the relaxation time is now defined as:

$$\bar{\tau}=\frac{\nu}{c_s^2}+\frac{\delta t}{2}. \quad (15)$$

The hydrodynamic pressure p_h is computed through the zeroth-order moment of the distribution function as:

$$p_h=\frac{c_s^2\delta t}{2}\left(u_i\frac{\partial\rho}{\partial x_i}+\rho\frac{\partial u_i}{\partial x_i}\right)+\sum_\alpha\bar{g}_\alpha, \quad (16)$$

while the velocity is defined as:

$$u_i=\frac{1}{\rho c_s^2}\sum_\alpha c_{\alpha,i}\bar{g}_\alpha+\frac{\delta t}{2}F_{b,i}. \quad (17)$$

For the sake of simplicity, the overbars on g_α and τ will be dropped in the remainder of the article.
The asymptotic analysis of this scheme and the corresponding macroscopic equations can be found in [56]. The velocity divergence appearing in Eqs. 14 and 16 is computed as:

$$\frac{\partial u_i}{\partial x_i}=\frac{1}{\bar{r}T}\left(\frac{\partial\bar{r}T}{\partial t}+u_i\frac{\partial\bar{r}T}{\partial x_i}\right)-\frac{1}{p_{th}}\frac{dp_{th}}{dt}, \quad (18)$$

with :

$$\bar{r}=\frac{R}{\bar{M}}, \quad (19)$$

where T is the temperature, and $\bar{M}$ is the mass-averaged molar mass computed as:

$$\frac{1}{\bar{M}}=\sum_k^{N_{sp}}\frac{Y_k}{M_k}, \quad (20)$$

where Y_k and M_k are the mass fraction and molar mass of species k and N_{sp} is the total number of species. Using Eq. 19, Eq. 18 can be further expanded as:

$$\frac{\partial u_i}{\partial x_i} = \frac{1}{T}\left(\frac{\partial T}{\partial t} + u_i\frac{\partial T}{\partial x_i}\right) + \sum_k^{N_{sp}} \frac{\bar{M}}{M_k}\left(\frac{\partial Y_k}{\partial t} + u_i\frac{\partial Y_k}{\partial x_i}\right) - \frac{1}{p_{th}}\frac{dp_{th}}{dt}. \quad (21)$$

Contrary to the weakly compressible LB model, here the local density is not an independent variable. It is computed from the temperature through the ideal gas equation:

$$\rho = \frac{p_{th}}{\bar{r}T}. \quad (22)$$

2.2. Energy and species fields

Writing the conservation equation for sensible enthalpy one gets, neglecting higher-order effects [60]:

$$\rho\left(\frac{\partial h_s}{\partial t} + u_i\frac{\partial h_s}{\partial x_i}\right) - \left(\frac{\partial p}{\partial t} + u_i\frac{\partial p}{\partial x_i}\right) - \frac{\partial}{\partial x_i}\left(\lambda\frac{\partial T}{\partial x_i}\right) + \frac{\partial}{\partial x_i}\left(\rho\sum_k^{N_{sp}} Y_k h_{s,k} V_{k,i}\right) - \mu\left(\frac{\partial u_i}{\partial x_j} + \frac{\partial u_j}{\partial x_i}\right)\frac{\partial u_i}{\partial x_j} = \dot{\omega}_T, \quad (23)$$

where h_s is the sensible enthalpy per unit mass of the mixture defined as $h_s = h - \sum_k^{N_{sp}} Y_k h_k(T_0)$, λ the thermal conductivity and $\dot{\omega}_T$ the heat release rate due to combustion defined as $\dot{\omega}_T = -\sum_k^{N_{sp}} h_k(T_0)\dot{\omega}_k$, where $\dot{\omega}_k$ is the k^{th} species mass production rate per unit volume. In the context of the LMNA, Eq. 23 can be re-written as:

$$\left(\frac{\partial T}{\partial t} + u_i\frac{\partial T}{\partial x_i}\right) = \frac{\bar{r}T}{\partial_T h_s}\frac{dp_{th}}{p_{th}dt} + \frac{1}{\rho\partial_T h_s}\frac{\partial}{\partial x_i}\left(\lambda\frac{\partial T}{\partial x_i}\right) - \frac{1}{\partial_T h_s}\left(\sum_k^{N_{sp}} \partial_T(h_{s,k}) Y_k V_{k,i}\right)\frac{\partial T}{\partial x_i} + \frac{\dot{\omega}_T}{\rho\partial_T h_s}, \quad (24)$$

where $\partial_T h_s$ and $\partial_T h_{s,k}$ can be replaced with the mixture and species specific heat capacities at constant pressure, c_p and $c_{p,k}$.
The species transport equation can be written as [60]:

$$\rho\left(\frac{\partial Y_k}{\partial t} + u_i\frac{\partial Y_k}{\partial x_i}\right) + \frac{\partial}{\partial x_i}\left(\rho Y_k V_{k,i}\right) = \dot{\omega}_k, \quad (25)$$

where $\mathbf{V}_k$ is the species diffusion velocity vector. The diffusion velocity is ideally computed from the Maxwell-Stefan system of equations [34, 52, 60, 61]. This system of equations being rather time-consuming to solve at each node and

time-step, simpler approximations are used instead. One of the approximations commonly used in combustion is the Hirschfelder-Curtiss approximation with a correction for the diffusion velocity. In the context of this approximation the diffusion velocity is defined as [60]:

$$Y_k V_{k,i} = -\frac{\mathcal{D}_k Y_k}{X_k}\frac{\partial X_k}{\partial x_i} + Y_k V_{c,i}, \tag{26}$$

where $\mathcal{D}_k$ is the effective diffusion coefficient and X_k is the mole fraction of species k and $\mathbf{V}_c$ the diffusion velocity correction. The mole fraction is related to the mass fraction through:

$$\frac{Y_k}{X_k} = \frac{M_k}{\bar{M}}. \tag{27}$$

Using Eq. 27, Eq. 26 can be re-written as:

$$Y_k V_{k,i} = -\frac{\mathcal{D}_k M_k}{\bar{M}}\frac{\partial X_k}{\partial x_i} + Y_k V_{c,i}. \tag{28}$$

In order to guarantee mass conservation one must have:

$$\sum_k^{N_{sp}} Y_k V_{k,i} = 0. \tag{29}$$

Under this condition the diffusion velocity correction should be defined as:

$$V_{c,i} = \sum_k^{N_{sp}} \frac{\mathcal{D}_k M_k}{\bar{M}}\frac{\partial X_k}{\partial x_i}. \tag{30}$$

It is also worth mentioning that even simpler approximations are also frequently used. One of these approximations, used later for the first free-flame test-case as well as for the 2-D and 3-D counter-flow simulations, is the Fick approximation where the diffusion velocity $\mathbf{V}_k$ is computed as:

$$Y_k V_{k,i} = -\mathcal{D}_k \frac{\partial Y_k}{\partial x_i}. \tag{31}$$

In the context of the present study, both convection and diffusion terms in the species and energy balance equations are discretized using a second-order, central FD approximation in space, while to update the corresponding fields a first-order explicit Euler discretization is used in time.

For the 1-D test-case involving detailed thermo-chemistry (detailed kinetics, thermodynamic and transport properties) all parameters (local mixture-average specific heat capacity, effective diffusion coefficients etc) are evaluated using the in-house library REGATH. A detailed description of the models and equations can be found in [34].

2.3. Overall structure of the code

The code consists of three main building blocks, namely 1) a module to evaluate thermodynamics and transport properties, 2) the lattice Boltzmann LMNA solver for the flow field, and 3) an FD module for solving the species and temperature fields. The overall code structure is depicted in Fig. 1. At the beginning of each time-step, first thermo-chemical parameters (production rates, heat capacity and average molar mass) are evaluated at each node. Then, these parameters are used to compute the transport properties, i.e. the diffusion coefficients for momentum, energy and species. Once all parameters have been evaluated, the left-hand side of the species and energy transport equations are evaluated, and used to compute the divergence of the velocity field using Eq. 21, as well as temperatures and mass fractions at the next time-step. Using the obtained divergence, the flow solver populations are updated (collision, streaming and subsequent application of boundary conditions) and finally used to get the zeroth and first-order moments.

3. Validation of the hybrid solver

To validate the proposed scheme and showcase its performance, two classes of test-cases are considered. First, pseudo 1-D freely propagating flames with simple and detailed thermo-chemistry are modeled. Then, to demonstrate the ability of the proposed algorithm to deal with more realistic geometrical configurations, 2-D and 3-D flames are modeled.

3.1. Pseudo 1-D freely propagating flame-front

3.1.1. Simple thermo-chemistry: Propane/Air 1-D freely propagating flame-front

A 1-D freely-propagating Air/Propane premixed flame is first considered. This configuration consists of a 2-D simulation domain bounded by an inlet and outlet boundary condition in the x-direction and periodic boundary conditions (with only two grid-points)in the y-direction. At the inlet, a given mass flow-rate with a fixed temperature and composition is imposed through a fixed-velocity boundary condition on the flow solver and a set of Dirichlet boundary conditions on the temperature and species solvers. These boundary conditions correspond to the fresh gas composition. At the outlet, to emulate open-boundary conditions, constant hydrodynamic pressure – for the flow-field solver – and Neumann first-order zero-gradient boundary conditions – for the species and temperature fields, are enforced.
The simulations are initialized by imposing respectively fresh and burnt gas composition, temperature and density on the left and right half of the domain. Taking into account all time-step and grid-size restrictions emanating from the different solvers, namely: a lower and upper bound on the Fourier number Fo= $\frac{D\delta t}{\delta x^2}$ brought about respectively by the LB and FD solvers, an upper bound on time-step due to the stiffness of the chemical reaction terms, and finally an upper bound on the Courant–Friedrichs–Lewy (CFL) number $\frac{u_{max}}{\delta x/\delta t}$ tied to the

stability of the LB solver, the time-step and grid-size were set to $\delta t = 5 \times 10^{-8}$s and $\delta x = 1.55 \times 10^{-5}$m, respectively. It is worth mentioning that the generic parameter D appearing in the definition of the Fourier number is the parameter controlling diffusion in each solver, namely the viscosity, species diffusion coefficients, and thermal diffusivity, respectively. The simulations were performed over a 6.2 cm long domain in x-direction.
For this test-case, the Fick approximation is used to model species mass diffusion, while the dynamic viscosity is approximated through a Sutherland model following [44];

$$\mu = \mu(T^*)\left(\frac{T}{T^*}\right)^{\beta}, \tag{32}$$

where T^* – here taken to be 298 K –is a reference temperature, independent from the temperature used for the non-dimensionalisation of the heat transport equation, $\mu(T^*)$ is the dynamic viscosity at this temperature and β is a parameter set to 0.69 [44]. The thermal and species diffusion coefficients are determined through fixed Prandtl and Schmidt numbers given in Table 1.

Parameter	value
Pr	0.682
$Sc_{C_3H_8}$	1.241
Sc_{O_2}	0.728
Sc_{H_2O}	0.941
Sc_{CO_2}	0.537
Sc_{N_2}	0.682

Table 1: Prandtl and Schmidt numbers used for the 1-D Propane/Air simulations

For the sake of simplicity, the mixture heat capacity is taken to be constant and equal to 1008 J/kg.K.
The chemistry is described through a one-step global reaction:

$$C_3H_8 + 5\,(O_2 + \gamma N_2) \longrightarrow 3CO_2 + 4H_2O + 5\gamma N_2$$

and an Arrhenius-type forward reaction rate, $k_f = kT^{\beta}e^{-\frac{E_a}{RT}}$, where the reaction rate constant k, the activation energy E_a and the constant β are respectively set to $9.9 \times 10^{-7}\mathrm{m}^3.\mathrm{mol}^{-1}\mathrm{s}^{-1}$, 125520 J and 0. Furthermore, the overall heat of reaction is taken to be equal to 2.0×10^6J/mol [44, 30].
The simulations were ran for a range of equivalence ratio $\phi = \frac{\left(Y_{C_3H_8}/Y_{O_2}\right)}{\left(Y_{C_3H_8}/Y_{O_2}\right)_{st}}$– going from 0.5 to 1. The obtained results were assessed by comparing the adiabatic flame temperatures and flame propagation speeds to results reported in [44]. The flame propagation speed was computed by following the position of the flame-front–taken to be the position of the production-rate maxima. The obtained results for flame propagation speed and adiabatic flame temperature are shown in Fig. 2. Furthermore, the species and temperature profiles are also

compared to results from [44] in Fig 3. The results obtained by the developed LB-FD code are in very good agreement with those reported in [44]. To better showcase the effect of the temperature and species fields on the flow solver, the density and velocity profiles are also shown separately in Fig. 4.

3.1.2. Detailed thermo-chemistry: Methane/Air 1-D freely-propagating flame

As a proof of concept, and in order to show that the proposed model can be used with any type of formulation (also for multi-component diffusion and complex chemistry), results for an additional 1-D free-flame configuration are shown here. The case presented in this section is that of a premixed pseudo 1-D Methane/Air freely-propagating flame at an equivalence ratio of 1. The reduced chemical scheme is made of 7 chemical species and 4 reactions and is based on [62]:

$$CH_4 + \frac{1}{2}O_2 \longrightarrow CO + 2H_2$$

$$CH_4 + H_2O \longrightarrow CO + 3H_2$$

$$H_2 + \frac{1}{2}O_2 \rightleftharpoons H_2O$$

$$CO + H_2O \rightleftharpoons CO_2 + H_2$$

At the inlet (left side) a constant flow rate of fresh gas at room temperature is applied while at the outlet (right side) zero-gradient boundary conditions are applied to the species and energy fields while a constant hydrodynamic pressure is enforced on the flow field. For this test-case, detailed thermo-chemical properties, as reported and detailed in [34] are used in conjunction with the Hirschfelder-Curtiss approximation with a correction velocity for the species diffusion term. Thermodynamics and transport properties are handled using an in-house code, REGATH, coupled to the in-house LB solver, ALBORZ. The simulation was performed over a domain of size 80 mm. The simulation domain was spanned with 8000 grid-points with $\delta x = 1 \times 10^{-5}$ m and $\delta t = 1 \times 10^{-9}$ s. Given the stiffness of the reaction terms involved in the present chemical scheme, an IMPLEX (Implicit-Explicit) approach was used for the species and energy equations. The source terms were evaluated using a 5^{th} -order Runge-Kutta implicit solver (RADAU5) [63] while the remainder of the terms were advanced in time using a forward Euler scheme. The species profiles, as obtained from simulations with the hybrid solver are compared to their reference counterparts from [62] in Fig. 5. The agreement is excellent.

3.1.3. Order of accuracy: Methane/Air 1-D freely-propagating flame with BFER scheme

To assess the overall order of accuracy of the proposed solver, a 1-D freely propagating Methane/Air flame (similar to the previous test-case) is modeled using the BFER 2-step chemistry model [64]. The two-step chemical reactions are:

$$CH_4 + \frac{3}{2}O_2 \longrightarrow CO + 2H_2O$$

$$\mathrm{CO} + \frac{1}{2}\mathrm{O_2} \rightleftharpoons \mathrm{CO_2}$$

Corresponding reaction rates can be found in [64]. Detailed transport and thermodynamic properties are used for this simulation. The physical size of the domain is 1 cm. Initially, the domain is divided into two equal-sized sections. The left-hand side is initialized using fresh gas while the right-hand side is filled with burnt gas. The initial conditions are given in Table 2. Similar to the previous test-cases, at the inlet fresh gas composition, temperature and density are imposed along with constant velocity, while the outlet is modeled using zero-gradient boundary conditions.

Parameter	fresh gas	burnt
$T[K]$	800	2230
$u[m/s]$	0	0
Y_{CH_4}	0.0393	0
Y_{O_2}	0.2239	0.0682
Y_{H_2O}	0	0.0883
Y_{CO_2}	0	0.1046
Y_{CO}	0	2.01×10^{-3}

Table 2: Methane/Air BFER free flame initial conditions

Simulations were performed using five different grid-sizes, namely 10^{-5}, 1.5×10^{-5}, 2×10^{-5}, 3×10^{-5} and 4×10^{-5}m. The time-steps determined based on diffusive scaling were taken as: 5×10^{-9}, 1.125×10^{-8}, 2×10^{-8}, 4.5×10^{-8} and 8×10^{-8}s, respectively.

After convergence, the flame-front propagation speeds were measured and corresponding errors (as compared to a reference REGATH simulation) were computed. The obtained results are shown in Fig. 6. As can be observed, the overall solver shows second-order convergence behavior in space. This is in agreement with the order of each individual solver, and of the coupling scheme.

3.2. Multi-dimensional configurations

3.2.1. 2-D configuration I: premixed Propane/Air counter flow flame

The next test-case considered here, is that of a 2-D premixed counter-flow burner. The corresponding geometry is represented in Fig. 7. As shown there, at the inlets, the fresh gas mixture comes in at a constant velocity (therefore constant mass flow-rate), an equivalence ratio of $\phi = 0.6$ and a constant temperature of 300 K, and at the outlets (left and right) a constant hydrodynamic pressure is imposed on the flow field while the species and temperature fields are subjected to zero-gradient boundary conditions. At solid walls, zero diffusive flux is imposed on both the temperature and species fields. The simulation is initialized with fresh gas in the blank region in Fig.7 while the grey-colored region is filled with burnt gas. In the simulations, due to the symmetrical configuration of the burner, only the upper right quadrant is considered. The chemical

Parameter	fresh gas	burnt
$T[K]$	300	1970
$\rho[kg/m^3]$	1.17	0.162
$u[m/s]$	0	0
$Y_{C_3H_8}$	0.037	0
Y_{O_2}	0.224	0
Y_{H_2O}	0	0.061
Y_{CO_2}	0	0.111

Table 3: 2-D counter-flow burner initial conditions

scheme, thermodynamic and transport properties follow those set in subsection 3.1.1. The test-case is modeled using both the proposed hybrid scheme, and the commercial CFD solver ANSYS-FLUENT for comparison. The initial conditions are given in Table 3. The background thermodynamic pressure in both solvers is set to atmospheric pressure.
In FLUENT, the pressure-based solver is used to model the previously defined flow on a uniform grid of size $\delta x = 2 \times 10^{-5}$m. The correlations for viscosity, thermal conductivity, and species diffusion coefficients are imposed using external user-defined functions. The inlet and outlet are respectively modeled using the constant velocity and outflow boundary conditions.
In the LB-FD simulation, the D2Q9 stencil is used, while the grid and time-step sizes are respectively set to $\delta x = 5.55 \times 10^{-5}$m and $\delta t = 5 \times 10^{-7}$s. The inlet, walls and outlet boundary conditions are imposed using a modified version of the non-equilibrium extrapolation method, while the symmetry boundary conditions are applied using the classical approach, given in details in [1].
For the non-equilibrium extrapolation boundary conditions [65], the missing population at the boundary node are computed as:

$$g_\alpha\left(\boldsymbol{x_w}, t+\delta t\right) = g_\alpha^{(eq)}\left(\boldsymbol{x_w}, t+\delta t\right) + g_\alpha\left(\boldsymbol{x_w}+\mathbf{n}, t+\delta t\right) - g_\alpha^{(eq)}\left(\boldsymbol{x_w}+\boldsymbol{n}, t+\delta t\right), \quad (33)$$

where $\boldsymbol{n}$ is the inward pointing vector perpendicular to the boundary surface. For velocity boundary condition, $g_\alpha^{(eq)}\left(\boldsymbol{x_w}, t+\delta t\right)$ and $g_\alpha^{(eq)}\left(\boldsymbol{x_w}+\boldsymbol{n}, t+\delta t\right)$ are defined as:

$$g_\alpha^{(eq)}\left(\boldsymbol{x_w}+\boldsymbol{n}\right) = w_\alpha\left(p_h(\boldsymbol{x_w}+\boldsymbol{n}) - c_s^2\rho(\boldsymbol{x_w}+\boldsymbol{n})\right) + c_s^2 f_\alpha^{(eq)}\left(\rho(\boldsymbol{x_w}+\boldsymbol{n}), \boldsymbol{u}(\boldsymbol{x_w}+\boldsymbol{n})\right), \quad (34)$$

where the hydrodynamic pressure, density and velocity at $\boldsymbol{x_w}+\boldsymbol{n}$ can be computed as all populations are known:

$$g_\alpha^{(eq)}\left(\boldsymbol{x_w}\right) = w_\alpha\left(p_h(\boldsymbol{x_w}+\boldsymbol{n}) - c_s^2\rho(\boldsymbol{x_w})\right) + c_s^2 f_\alpha^{(eq)}\left(\rho(\boldsymbol{x_w}), \boldsymbol{u}(\boldsymbol{x_w})\right). \quad (35)$$

In both equations, the local hydrodynamic pressure is approximated by the neighbor node pressure, the velocity is imposed, and the temperature is computed from the local temperature and composition (through the ideal gas law). For the pressure boundary condition, the last equation is replaced by:

$$g_\alpha^{(eq)}\left(\boldsymbol{x_w}\right) = w_\alpha\left(p_h(\boldsymbol{x_w}) - c_s^2\rho(\boldsymbol{x_w})\right) + c_s^2 f_\alpha^{(eq)}\left(\rho(\boldsymbol{x_w}), \boldsymbol{u}(\boldsymbol{x_w}+\boldsymbol{n})\right). \quad (36)$$

At steady-state, the solutions obtained using both codes are compared. First, the density and Propane net production rates are compared in Fig. 8; these quantities can be used to identify the position of the flame front. As observed in this figure, there is an excellent agreement concerning position and shape of the flame fronts for both solvers. Furthermore, to verify that the thermal dilatation effect is correctly captured, the y-component of the velocity vectors along the vertical center-line are compared for both codes in Fig. 9. It is readily observed that the proposed hybrid scheme is able to correctly capture thermo-compressible effects.

3.2.2. 2-D configuration II: co-current jet Methane/Air diffusion flame

To illustrate the ability of the proposed algorithm to deal with diffusion flames, a laminar co-flow Methane/Air diffusion flame is considered here. The simulation uses the same thermo-chemical settings as those used in subsection 3.1.3. The geometrical configuration along with boundary conditions are given in Fig. 10 and Table 4. The fuel is injected at the center while the oxydant comes in from the sides. In the context of this study only the right-half of domain is modeled, and a symmery boundary condition is applied on the left-hand side. The time-step and grid-sizes were respectively set to $\delta t = 5 \times 10^{-8}$

Parameter	central inlet	left/right inlets
$T[K]$	950	950
$u_0[m/s]$	0.3	0.3
$Y_{C_3H_8}$	0.1	0
Y_{O_2}	0	0.224
Y_{H_2O}	0	0
Y_{CO_2}	0	0
Y_{CO}	0	0

Table 4: 2-D counter-flow burner initial conditions

s and $\delta x = 2.5 \times 10^{-5}$ m. The temperature, CO and CO_2 mass fraction fields are shown in Fig. 11. The results obtained from this simulation are compared to their counterpart from FLUENT in Fig. 12.

3.2.3. 3-D configuration: premixed Propane/Air counter flow flame

The last test-case considered here, is the 3-D version of the previously discussed 2-D counter-flow premixed flame. All parameters and boundary conditions are similar to the previous case. The corresponding geometry in 3-D

is shown in Fig 13. For the 3-D simulation in LB, the D3Q27 stencil is used while the grid and time-step sizes are respectively set to $\delta x = 1.67 \times 10^{-4}$m and $\delta t = 6 \times 10^{-6}$s, leading to a simulation domain of $200 \times 200 \times 120$ grid points. The pressure outlet, velocity inlet and wall boundary conditions are applied through the modified non-equilibrium extrapolation scheme, similar to the previous 2-D simulation. The computation was performed in parallel on the Neumann high-performance cluster at the university of Magdeburg, using 125 processing units. The steady-state fields obtained from the hybrid LB-FD simulation are displayed in Fig 14. In this figure, the flame front, represented by a Propane production rate iso-surface is shown in light gray, while the combustor walls are shown in darker gray. To validate the results, the temperature and species mass fractions, along with the z-component of the velocity vector along the central vertical line are compared to a pseudo 1-D simulation in cylindrical coordinates obtained from REGATH in Fig. **??**. Though the hybrid LB-simulation is 3-D while the solution from REGATH is 1D-axisymmetric, the distance from the vertical centerline to the domain boundaries is so large that the solutions are expected to closely agree. Indeed, as for all previous test-cases, the results obtained with the proposed hybrid LB-solver are in excellent agreement with their REGATH counterparts corresponding to a pure FD-approximation.

4. Conclusions and perspectives

A hybrid LB-FD solver for low Mach number combustion has been developed. The different test-cases studied here have shown that the proposed scheme is able to correctly recover the physics of low Mach flames. This is true for simple as well as for detailed thermo-chemical models; in 1-D, 2-D, and 3-D configurations; and considering geometries with different levels of complexity. To the knowledge of the authors this is the first time that results are published for 3-D combustion simulations taking into account thermo-compressibility using (in part or entirely) the LB method. Application of the proposed model to turbulent combustion is the topic of our present research.

5. acknowledgments

The financial support of the German research foundation (DFG), Germany within the graduate college for "Micro-Macro-Interactions in Structured Media and Particle Systems" (GRK 1554) is gratefully acknowledged. The authors would also like to thank the reviewers for their insightful comments.

References

References

[1] T. Krüger, H. Kusumaatmaja, A. Kuzmin, O. Shardt, G. Silva, E. M. Viggen, The lattice boltzmann method, Springer International Publishing 10 (2017) 978–3.

[2] L. Wang, J. Mi, X. Meng, Z. Guo, A localized mass-conserving lattice boltzmann approach for non-newtonian fluid flows, Communications in Computational Physics 17 (4) (2015) 908–924.

[3] A. Eshghinejadfard, S. A. Hosseini, D. Thévenin, Fully-resolved prolate spheroids in turbulent channel flows: a lattice Boltzmann study, AIP Advances 7 (9) (2017) 095007.

[4] R. H. H. Abadi, M. H. Rahimian, A. Fakhari, Conservative phase-field lattice-Boltzmann model for ternary fluids, Journal of Computational Physics 374 (2018) 668–691.

[5] M. Wöhrwag, C. Semprebon, A. M. Moqaddam, I. Karlin, H. Kusumaatmaja, Ternary free-energy entropic lattice boltzmann model with a high density ratio, Physical Review Letters 120 (23) (2018) 234501.

[6] H. Amirshaghaghi, M. H. Rahimian, H. Safari, M. Krafczyk, Large eddy simulation of liquid sheet breakup using a two-phase lattice boltzmann method, Computers & Fluids 160 (2018) 93–107.

[7] H. Safari, M. H. Rahimian, M. Krafczyk, Consistent simulation of droplet evaporation based on the phase-field multiphase lattice Boltzmann method, Phys. Rev. E 90 (2014) 033305.

[8] S. Succi, G. Bella, F. Papetti, Lattice kinetic theory for numerical combustion, Journal of Scientific Computing 12 (4) (1997) 395–408.

[9] D. d'Humières, Generalized lattice-Boltzmann equations, Prog. Astronaut. Aeronaut. 159 (1992) 450–458.

[10] P. Lallemand, L.-S. Luo, Theory of the lattice Boltzmann method: Dispersion, dissipation, isotropy, galilean invariance, and stability, Phys. Rev. E 61 (2000) 6546–6562.

[11] M. Geier, A. Greiner, J. G. Korvink, Cascaded digital lattice Boltzmann automata for high Reynolds number flow, Phys. Rev. E 73 (2006) 066705.

[12] M. Geier, A. Greiner, J. G. Korvink, A factorized central moment lattice Boltzmann method, Eur. Phys. J. Spec. Top. 171 (1) (2009) 55–61.

[13] F. Dubois, T. Février, B. Graille, On the stability of a relative velocity lattice Boltzmann scheme for compressible Navier–Stokes equations, C. R. Mécanique 343 (10) (2015) 599 – 610.

[14] A. De Rosis, K. H. Luo, Role of higher-order Hermite polynomials in the central-moments-based lattice Boltzmann framework, Phys. Rev. E 99 (2019) 013301.

[15] M. Geier, M. Schönherr, A. Pasquali, M. Krafczyk, The cumulant lattice Boltzmann equation in three dimensions: Theory and validation, Comput. Math. Appl. 70 (4) (2015) 507 – 547.

[16] M. Geier, A. Pasquali, M. Schönherr, Parametrization of the cumulant lattice Boltzmann method for fourth order accurate diffusion part I: Derivation and validation, J. Comput. Phys. 348 (Supplement C) (2017) 862 – 888.

[17] M. Geier, A. Pasquali, M. Schönherr, Parametrization of the cumulant lattice Boltzmann method for fourth order accurate diffusion part II: Application to flow around a sphere at drag crisis, J. Comput. Phys. 348 (Supplement C) (2017) 889 – 898.

[18] M. Geier, A. Pasquali, Fourth order Galilean invariance for the lattice Boltzmann method, Comput. Fluids 166 (2018) 139 – 151.

[19] J. Latt, B. Chopard, Lattice Boltzmann method with regularized pre-collision distribution functions, Math. Comput. Simul. 72 (2-6) (2006) 165–168.

[20] H. Chen, R. Zhang, I. Staroselsky, M. Jhon, Recovery of full rotational invariance in lattice Boltzmann formulations for high Knudsen number flows, Physica A 362 (1) (2006) 125–131.

[21] I. V. Karlin, A. Ferrante, H. C. Öttinger, Perfect entropy functions of the lattice Boltzmann method, Europhys. Lett. 47 (2) (1999) 182–188.

[22] B. M. Boghosian, J. Yepez, P. V. Coveney, A. Wager, Entropic lattice Boltzmann methods, Proc. Royal Soc. A 457 (2007) (2001) 717–766.

[23] S. Arcidiacono, J. Mantzaras, I. Karlin, Lattice Boltzmann simulation of catalytic reactions, Physical Review E 78 (4) (2008) 046711.

[24] J. Kang, N. I. Prasianakis, J. Mantzaras, Lattice Boltzmann model for thermal binary-mixture gas flows, Physical Review E 87 (5) (2013) 053304.

[25] J. Kang, N. I. Prasianakis, J. Mantzaras, Thermal multicomponent lattice Boltzmann model for catalytic reactive flows, Physical Review E 89 (6) (2014) 063310.

[26] C. Lin, K. H. Luo, L. Fei, S. Succi, A multi-component discrete boltzmann model for nonequilibrium reactive flows, Scientific reports 7 (1) (2017) 14580.

[27] C. Lin, K. H. Luo, MRT discrete Boltzmann method for compressible exothermic reactive flows, Computers & Fluids 166 (2018) 176–183.

[28] C. Lin, K. H. Luo, Discrete Boltzmann modeling of unsteady reactive flows with nonequilibrium effects, Physical Review E 99 (1) (2019) 012142.

[29] C. Lin, K. H. Luo, Mesoscopic simulation of nonequilibrium detonation with discrete boltzmann method, Combustion and Flame 198 (2018) 356–362.

[30] K. Yamamoto, X. He, G. D. Doolen, Simulation of combustion field with lattice Boltzmann method, Journal of Statistical Physics 107 (1-2) (2002) 367–383.

[31] S. Chen, Z. Liu, Z. Tian, B. Shi, C. Zheng, A simple lattice Boltzmann scheme for combustion simulation, Computers & Mathematics with Applications 55 (7) (2008) 1424–1432.

[32] E. Chiavazzo, I. V. Karlin, A. N. Gorban, K. Boulouchos, Coupling of the model reduction technique with the lattice Boltzmann method for combustion simulations, Combustion and Flame 157 (10) (2010) 1833–1849.

[33] E. Chiavazzo, I. V. Karlin, A. N. Gorban, K. Boulouchos, Combustion simulation via lattice Boltzmann and reduced chemical kinetics, Journal of Statistical Mechanics: Theory and Experiment 2009 (06) (2009) P06013.

[34] S. A. Hosseini, A. Eshghinejadfard, N. Darabiha, D. Thévenin, Weakly compressible lattice boltzmann simulations of reacting flows with detailed thermo-chemical models, Computers & Mathematics with Applications (2017). doi:10.1016/j.camwa.2017.08.045.

[35] S. A. Hosseini, N. Darabiha, D. Thévenin, Mass-conserving advection–diffusion lattice Boltzmann model for multi-species reacting flows, Physica A: Statistical Mechanics and its Applications 499 (2018) 40–57.

[36] S. Hosseini, N. Darabiha, D. Thevenin, Lattice boltzmann advection-diffusion model for conjugate heat transfer in heterogeneous media, International Journal of Heat and Mass Transfer 132 (2019) 906–919.

[37] Z. Chai, X. Guo, L. Wang, B. Shi, Maxwell-Stefan-theory-based lattice Boltzmann model for diffusion in multicomponent mixtures, Physical Review E 99 (2) (2019) 023312.

[38] P. Lallemand, L.-S. Luo, Hybrid finite-difference thermal lattice Boltzmann equation, International Journal of Modern Physics B 17 (01n02) (2003) 41–47.

[39] A. Mezrhab, M. Bouzidi, P. Lallemand, Hybrid lattice-Boltzmann finite-difference simulation of convective flows, Computers & Fluids 33 (4) (2004) 623–641.

[40] S. A. Hosseini, N. Darabiha, D. Thévenin, A. Eshghinejadfard, Stability limits of the single relaxation-time advection–diffusion lattice Boltzmann scheme, International Journal of Modern Physics C 28 (12) (2017) 1750141.

[41] Y.-L. Feng, S.-L. Guo, W.-Q. Tao, P. Sagaut, Regularized thermal lattice boltzmann method for natural convection with large temperature differences, International Journal of Heat and Mass Transfer 125 (2018) 1379–1391.

[42] S. A. Hosseini, C. Coreixas, N. Darabiha, D. Thévenin, Stability of the lattice kinetic scheme and choice of the free relaxation parameter, Physical Review E 99 (6) (2019) 063305.

[43] P. J. Dellar, Bulk and shear viscosities in lattice Boltzmann equations, Physical Review E 64 (3) (2001) 031203.

[44] Y. Feng, M. Tayyab, P. Boivin, A lattice-Boltzmann model for low-Mach reactive flows, Combustion and Flame 196 (2018) 249–254.

[45] N. I. Prasianakis, I. V. Karlin, Lattice boltzmann method for thermal flow simulation on standard lattices, Physical Review E 76 (1) (2007) 016702.

[46] M. H. Saadat, F. Bösch, I. V. Karlin, Lattice boltzmann model for compressible flows on standard lattices: Variable prandtl number and adiabatic exponent, Physical Review E 99 (1) (2019) 013306.

[47] H. Grad, On the kinetic theory of rarefied gases, Communications on pure and applied mathematics 2 (4) (1949) 331–407.

[48] N. Frapolli, S. S. Chikatamarla, I. V. Karlin, Lattice kinetic theory in a comoving galilean reference frame, Physical Review Letters 117 (1) (2016) 010604.

[49] B. Dorschner, F. Bösch, I. V. Karlin, Particles on demand for kinetic theory, Physical Review Letters 121 (13) (2018) 130602.

[50] X. Li, Y. Shi, X. Shan, Temperature-scaled collision process for the high-order lattice Boltzmann model, Physical Review E 100 (1) (2019) 013301.

[51] S. Chen, Z. Liu, C. Zhang, Z. He, Z. Tian, B. Shi, C. Zheng, A novel coupled lattice boltzmann model for low mach number combustion simulation, Applied Mathematics and Computation 193 (1) (2007) 266–284.

[52] V. Giovangigli, Multicomponent flow modeling, Springer, 2012.

[53] M. Lai, J. Bell, P. Colella, A projection method for combustion in the zero mach number limit, in: 11th Computational Fluid Dynamics Conference, 1993, p. 3369.

[54] A. Abdelsamie, G. Fru, T. Oster, F. Dietzsch, G. Janiga, D. Thévenin, Towards direct numerical simulations of low-Mach number turbulent reacting and two-phase flows using immersed boundaries, Computers & Fluids 131 (2016) 123–141.

[55] O. Filippova, D. Hänel, A novel lattice BGK approach for low mach number combustion, Journal of Computational Physics 158 (2) (2000) 139–160.

[56] H. Safari, M. Krafczyk, M. Geier, A lattice Boltzmann model for thermal compressible flows at low mach numbers beyond the boussinesq approximation, Computers & Fluids (2018).

[57] T. Lee, Effects of incompressibility on the elimination of parasitic currents in the lattice Boltzmann equation method for binary fluids, Computers & Mathematics with Applications 58 (5) (2009) 987–994.

[58] T. Lee, L. Liu, Lattice Boltzmann simulations of micron-scale drop impact on dry surfaces, Journal of Computational Physics 229 (20) (2010) 8045–8063.

[59] K. Sun, S. Yang, C. K. Law, A diffuse interface method for simulating the dynamics of premixed flames, Combustion and Flame 163 (2016) 508–516.

[60] T. Poinsot, D. Veynante, Theoretical and numerical combustion, RT Edwards, Inc., 2005.

[61] R. Hilbert, F. Tap, H. El-Rabii, D. Thévenin, Impact of detailed chemistry and transport models on turbulent combustion simulations, Progress in Energy and Combustion Science 30 (1) (2004) 61–117.

[62] W. Jones, R. Lindstedt, Global reaction schemes for hydrocarbon combustion, Combustion and Flame 73 (3) (1988) 233–249.

[63] G. Wanner, E. Hairer, Solving ordinary differential equations II, Springer Berlin Heidelberg, 1996.

[64] B. Franzelli, E. Riber, L. Y. Gicquel, T. Poinsot, Large eddy simulation of combustion instabilities in a lean partially premixed swirled flame, Combustion and flame 159 (2) (2012) 621–637.

[65] G. Zhao-Li, Z. Chu-Guang, S. Bao-Chang, Non-equilibrium extrapolation method for velocity and pressure boundary conditions in the lattice Boltzmann method, Chinese Physics 11 (4) (2002) 366.

Figures

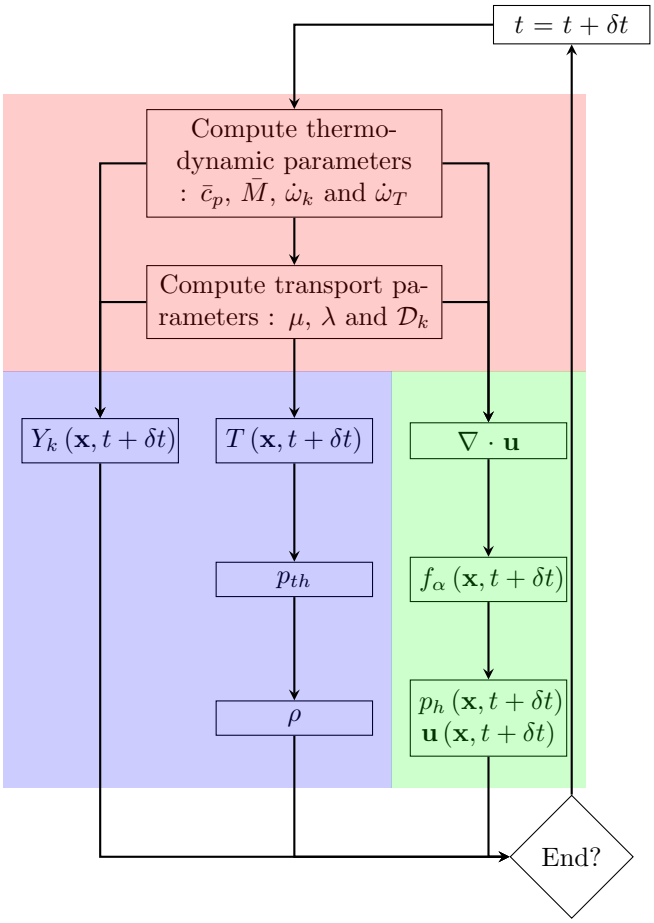

Figure 1: Overall structure of the proposed algorithm (in green the steps handled by the LB solver, in magenta those handled by the FD solver, and finally in red the thermo-chemistry module)

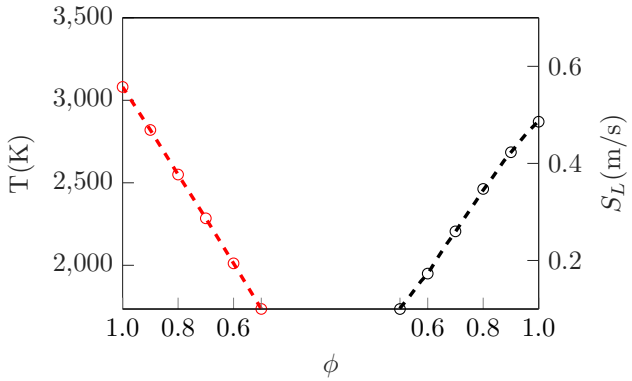

Figure 2: Adiabatic temperature (in red, left axis) and flame propagation speed (in black, right axis) obtained from the present hybrid LB-FD solver (- - -) compared to published reference data (○) from [44]

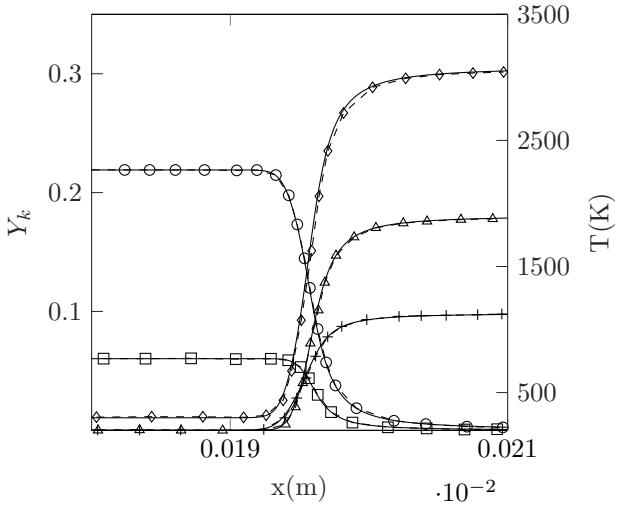

Figure 3: Species (left axis) and temperature (right axis) profiles obtained from hybrid LB-FD simulations shown with plain lines, compared to reference values from [44] shown with markers: (○) Y_{O_2}, (□) $Y_{C_3H_8}$, (+) Y_{H_2O}, (△) Y_{CO_2}, and (◇) temperature

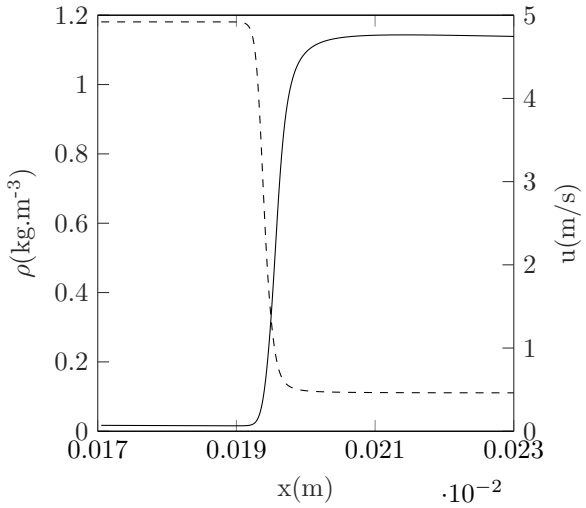

Figure 4: Density (left axis,- - -) and velocity profile (right axis, ——) distribution around the 1-D freely-propagating flame-front at ϕ=1

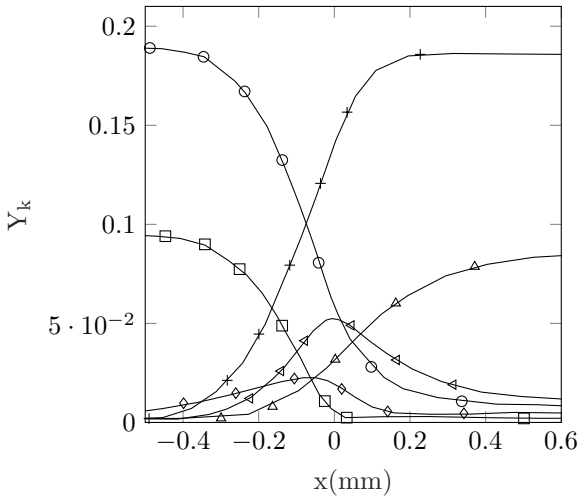

Figure 5: Species profiles around the flame-front from LB-FD simulations shown with plain lines compared to reference values from [62] shown with markers: (○) Y_{O_2}, (□) Y_{CH_4}, (+) Y_{H_2O}, (△) Y_{CO_2}, (◇) Y_{H_2}, (◁) Y_{CO}

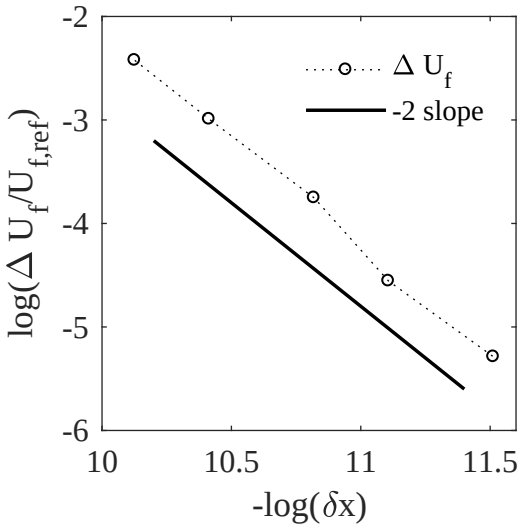

Figure 6: Methane/Air flame propagation speed error for different resolutions using the BFER scheme

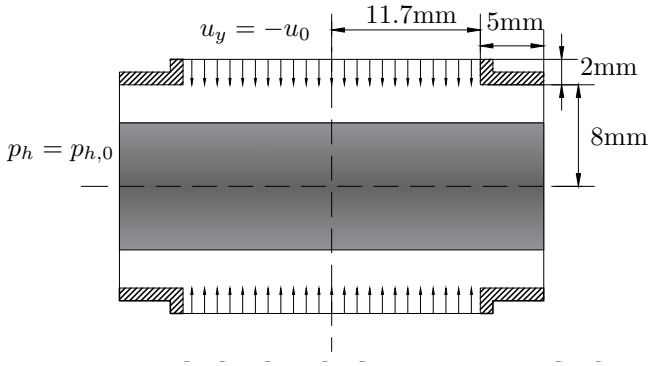

Figure 7: Geometrical configuration of the 2-D counter flow premixed Propane/Air flame. The grayed-out area is initially filled with burnt gas.

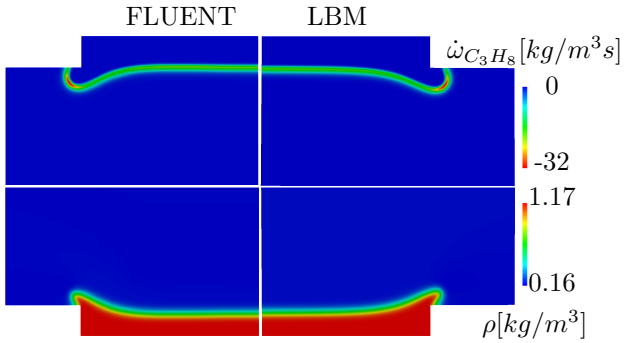

Figure 8: Density(lower half of the domain) and Propane net production rate (upper half of the domain) fields as obtained using FLUENT (left half) and the proposed Hybrid solver (right half).

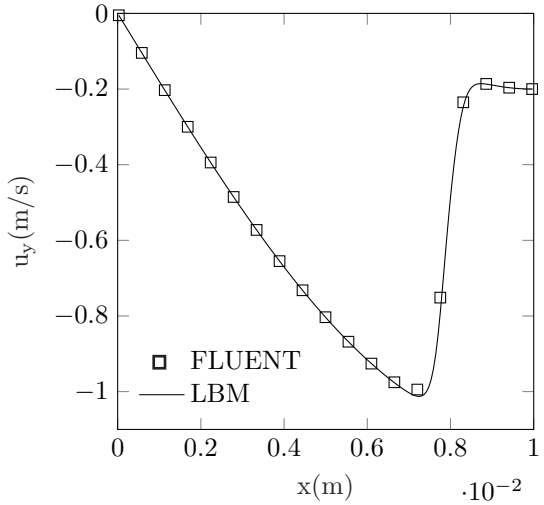

Figure 9: y-component of the velocity vector along the vertical center-line

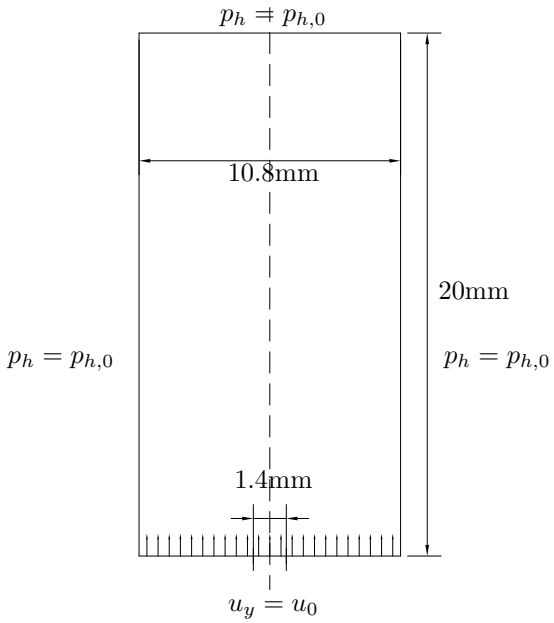

Figure 10: Geometrical configuration of the 2-D co-flow Methane/Air diffusion flame.

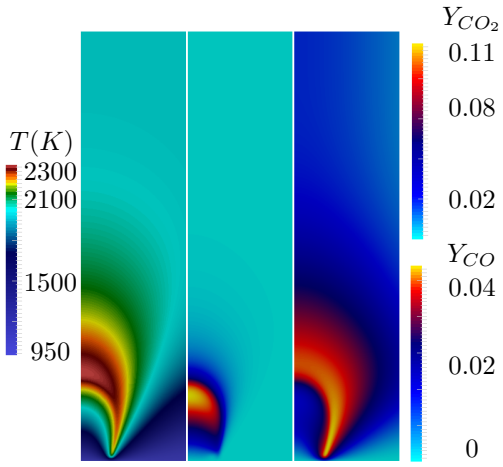

Figure 11: Temperature, CO and CO_2 mass fraction (from left to right) fields for co-flow diffusion flame

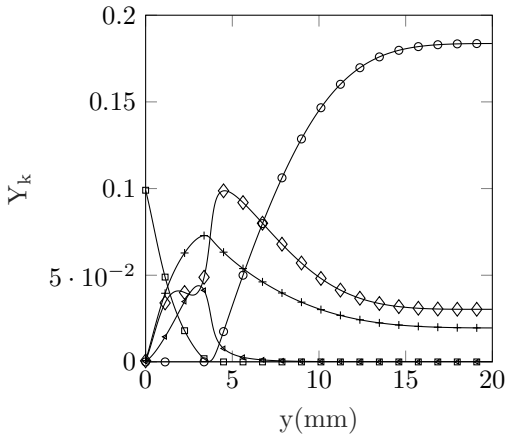

Figure 12: Species profiles obtained from FD-LB solver shown with solid lines, compared to results of FLUENT shown with markers: (○) Y_{O_2}, (□) Y_{CH_4}, (△) Y_{CO_2}, (◇) Y_{H_2}, (◁) Y_{CO}

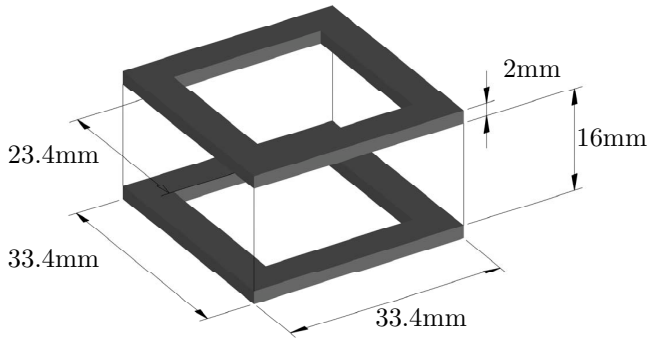

Figure 13: Geometrical configuration of the 3-D counter flow premixed Propane/Air flame.

Figure 14: Flow field obtained at steady-state for the 3-D counter-flow test-case. Shown in this figure: Iso-surface of Propane consumption rate $\dot{\omega}_{C_3H_8}$ in light gray; streamlines colored with velocity magnitude (see color scale); cut showing the z-component of the velocity vector in the central plane (see color scale)